

Micron-Scale Residual Stress Measurement by Micro-Hole Drilling and Digital Image Correlation

B. Winiarski · P.J. Withers

Received: 1 July 2010 / Accepted: 14 April 2011 / Published online: 6 May 2011
© Society for Experimental Mechanics 2011

Abstract This paper reports a new technique, namely the incremental micro-hole-drilling method (I μ HD) for mapping in-plane residual or applied stresses incrementally as a function of depth at the micron-scale laterally and the sub-micron scale depth-wise. Analogous to its macroscale counterpart, it is applicable either to crystalline or amorphous materials, but at the sub-micron scale. Our method involves micro-hole milling using the focused ion beam (FIB) of a dual beam FEGSEM/FIB microscope. The resulting surface displacements are recorded by digital image correlation of SEM images recorded during milling. The displacement fields recorded around the hole are used to reconstruct the stress profile as a function of depth. In this way residual stresses have been characterized around a drilled hole of 1.8 microns. diameter, enabling the profiling of the stress variation at the sub-micron scale to a depth of 1.8 microns. The new method is used to determine the near surface stresses in a (peened) surface-severe-plastically-deformed (S²PD) Zr₅₀Cu₄₀Al₁₀ (in atomic percent, at.%) bulk metallic glass bar. In plane principal stresses of -800 MPa \pm 90 MPa and -600 MPa \pm 90 MPa were measured, the maximum compressive stress being oriented 15° to the axis of the bar.

Keywords Scanning electron microscopy (SEM) · Residual stress · 2D digital image correlation · Surface decoration methods · Incremental centre hole drilling

Introduction

Residual stresses arise in most materials as a consequence of processing and/or in-service loading. Depending on their sign, magnitude, spatial distribution, and the scale over which they equilibrate, residual stresses can alter the mechanical and functional performance [1]. Consequently their quantification is of great importance across many sectors. Whilst there exists a plethora of techniques for measuring stress at the macroscale, few techniques allow micron scale evaluation, either laterally or with depth, especially for amorphous materials.

In theory, destructive and semi-destructive techniques based on mechanical relaxation phenomena, such as slitting [2, 3], hole/core drilling [4–11] and curvature methods [12] can be scaled down and applied to smaller structures [13–25] than those to which they have traditionally been applied. The advent of dual beam focused ion beam–field emission gun scanning electron microscopes (FIB-FEG-SEM) has, in combination with digital image correlation (DIC) analysis, made it possible to make very fine excisions and to record the resulting displacements with high precision, usually in the nanometre range. Recently, this has led to a number of micro-scale analogues of the mechanical stress measurement methods. For example, 0.28 μ m deep 10 \times 0.2 μ m slots have been used to measure the stresses in an amorphous diamond-like carbon coating [14], while stresses have been mapped at the micron scale in bulk metallic glasses using an array of such slots [20]. This method provides a measure of the stress normal to the slot averaged over the slot depth. Depth profiling has been achieved by monitoring beam deflection of micro-cantilevers as they are progressively milled [25]. However, for stress mapping it requires excavation of large micro-cantilevers (length of 100 μ m or more). Essentially both methods are based on 1-D

B. Winiarski (✉, SEM member) · P.J. Withers (SEM member)
School of Materials, Materials Science Centre,
The University of Manchester,
Grosvenor Street,
Manchester M1 7HS, UK
e-mail: b.winiarski@manchester.ac.uk



analyses, allowing only a single component of stress to be determined, with lateral spatial resolutions of many tens of microns. Other examples show that atomic force microscopy (AFM) in combination with DIC is capable of surface displacement field measurement in the nanometre range. This measurement method together with the microscopic through-hole method has been successfully applied to assess stresses and elastic properties of polycrystalline silicon micro electro-mechanical system (MEMS) devices [19].

A FIB microscope is capable of milling holes having diameters of tens of nanometers. Consequently, if the displacement measurement technique can be improved, further improvements in the miniaturization of the technique may be possible. The reliability of displacement/strain analysis of DIC-based measurement techniques when applied to FIB-based micro-hole milling depends strongly on the surface contrast. Since digital image correlation software compares gray-scale maps/patches, it is preferable that the digital images are characterized by random, high contrast features [26, 27]. At the macro-scale this can be achieved by polishing, etching, painting, etc. [28]. However at the micron-scale either the FIB can be used to apply markers (both ion and electron beam assisted deposition of metals e.g. Pt, W, Fe, Co, Au), or other surface decoration methods can be applied [20, 29, 30].

We demonstrate a new experimental technique, namely the incremental micro-hole-drilling method ($1\mu\text{HD}$), for local measurement of in-depth profiles of principal residual-stresses applicable to crystalline and amorphous materials. Our incremental method is similar to the micro-hole drilling method proposed by Vogel et al. [31], but can provide stress as a function of depth. It combines FIB micro-hole milling with two-dimensional (2-D) finite-element analysis (FEA) based on the hole geometry to model the resulting relaxation displacements on the specimen surface, as determined by DIC analysis. Compared to stress measurement by slotting or micro-cantilevers it has the advantages that a) holes can be very compact providing excellent lateral spatial resolution, b) small holes are relatively straightforward to drill, c) it provides the full in-plane stress tensor and d) it can provide good depth resolution. The challenge however is to measure the associated surface displacements which are much smaller than for the above techniques. Our approach adapts the Unit Pulse Method (UPM) [4, 5] combined with a Tikhonov regularization scheme [32, 33] and uses full-field radial displacement data for each hole-depth increment, from which the associated residual-stress profile is inferred. In this manner the method is appropriate for the estimation of highly non-uniform residual stress distributions and allows for stable residual-stress solution even when the small increments of depth are selected near to, or far from, the material surface. The incremental micro-hole drilling method is used to estimate

the residual-stresses profiles in a surface-severe-plastically-deformed bulk metallic glass (BMG) system to a depth resolution of ~ 200 nm and a lateral resolution of around $10\ \mu\text{m}$ based on a $4\ \mu\text{m}$ micro-hole.

Materials and Methods

Sample Preparation

The Zr-based $\text{Zr}_{50}\text{Cu}_{40}\text{Al}_{10}$ (atm%) BMG was prepared by arc-melting a mixture of pure zirconium, copper, and aluminum melts (purity better than 99.9% by weight) in an argon atmosphere. A tilt-casting method was implemented to cast the alloy to its final rod shape of 60 mm and diameter of 8 mm. The rod sample was cut to a rectangular bar of $3\times 3\times 25\text{mm}^3$ and, then, polished using the 600-grit grinding paper.

Subsequently, one side of the specimen was repeatedly bombarded in an argon atmosphere with twenty WC/Co balls, each having a diameter of 1.6 mm, using a Spex 8000 miller in a back-to-force mode with a frequency of 60 Hz. The bombardment process lasted for 180 minutes pausing every 15 minutes. This surface-severe-plastic-deformation (S^2PD) process has a much higher average impact energy than the shot-peening process, thereby generating a severely-deformed near-surface layer of thickness about $180\ \mu\text{m}$ in the BMG at room temperature, constrained by an elastically deformed region immediately below this. The near-surface layer which is about $30\text{--}40\ \mu\text{m}$ thick with an effective plastic deformation of about 10%–30%, contains a uniform distribution of sub-micron size shear bands (see [34] and references cited there). The near surface stress variation has been previously determined by micro-slotting and is similar to that characteristic of shot-peening profiles [20]. The peak compressive residual-stress is located within the microstructurally-affected layer at a depth of around $160\ \mu\text{m}$.

To enhance the accuracy of the DIC analysis, the specimen surface was decorated with 20–30 nm yttria-stabilized-zirconia (YSZ) equi-axed particles precipitated from an ethanol suspension (see Fig. 1), where the surface coverage is about 10%. To minimize any surface charging effects and to ‘protect’ the surface from Ga^+ implantation, the surface of the specimen was coated with a 22 nm thick carbon film using a Gatan PECS 682 etching-coating system equipped with a Gatan 681.20000 Thickness Meter. This decoration technique allowed us to work at magnifications of $10,000\times$ in FEGSEM mode viewing a surface area of tens of square microns [30].

Experimental Procedure

The two requirements for accurate DIC measurements of surface deformations are the presence of a fine and high-

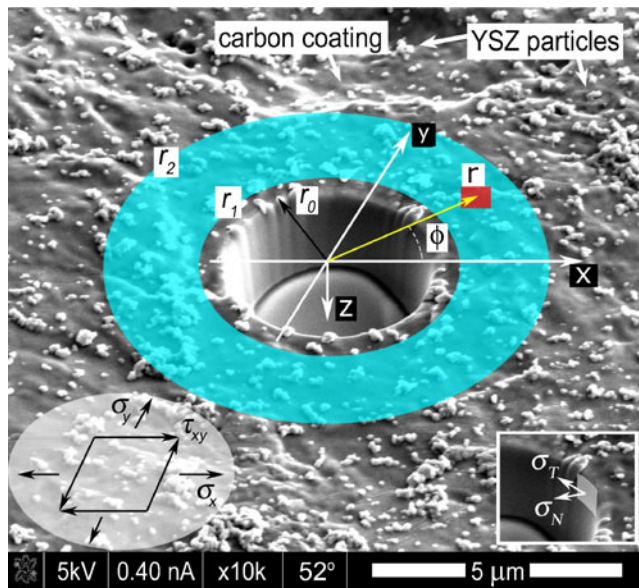


Fig. 1 (colour online) FEGSEM image of the microhole of diameter $d=4.0\pm 0.07\ \mu\text{m}$ and depth, $z=1.8\pm 0.07\ \mu\text{m}$; the surface has been decorated with YSZ nano-particles and then carbon coated

contrast surface texture, and the use of large correlation patch sizes [28, 35]. However, the imaging conditions used, namely voltage, current, dwell time, detection of secondary electrons (SE⁻) or back-scattered electrons (BE⁻), secondary ions (SI⁺), digital image resolution, etc., are also important [36, 37].

A series of FEGSEM imaging trials was performed to identify the optimal imaging conditions for DIC analysis. The control parameter chosen for minimization was the uncertainty of the DIC displacement (standard deviation of the displacement (SD_u)) mapped over the whole imaging area (here 1015 data points). It was found that an electron beam (e-beam) acceleration voltage of 5 kV, with beam current 0.40 nA, and detection of secondary electrons gives good contrast images with negligible charging of the sample surface. Subsequently, a range of e-beam dwell times (D_t) (D_t of 1 μs , 3 μs , 10 μs and 30 μs) and image acquisition conditions (image integration over 1, 4, 8 and 16 frames) were analyzed. All images were acquired after an auto-brightness/auto-contrast procedure. It was found that an e-beam dwell time of 3 μs and an integration over 8 frames (total image acquisition time = 21.7 s) gave the lowest SD_u (~0.0147 pixel) for DIC patches of 64×64 pixels overlapped by 75%.

An inherent feature of the FIB-milling process is material redeposition such that the milled walls are not perfectly rectangular, especially when milling deep holes or narrow slits. To limit such effects, the FIB-milled hole should be shallow. A diameter to depth ratio less than one is well matched to the inherent limitations associated with hole-milling experiments, whereby the magnitude of the

surface relaxations plateau as the contributions of stresses released at greater depths decline rapidly with the hole depth. In order to map the stress profile in a severely plastically deformed BMG, we have introduced a micro-hole of 2 μm radius to a depth of 1.8 μm (see Fig. 1) in 10 depth increments. This was achieved using a focused Ga⁺ ion beam of 0.28 nA accelerated by an electric field of 30 kV. The hole-irradiation process was done at a 52° angle, where the sample surface is normal to the ion column axis.

The surface displacements due to the stress relaxations were mapped by cross-correlation from the FEGSEM images (these are of much higher quality and do little beam damage compared to Ion Beam images) at each increment using DIC software (LaVision DaVis 7.2) [see Fig. 2(a)]. Each image was taken after tilting the sample stage to the 0° position. The first FEGSEM image was taken for the imaged region without the hole, and was used as the reference image for the cross-correlation analysis. The DIC patches (64×64 pixels overlapped by 75%) covered the whole imaged area apart from the micro-hole and its immediate vicinity (within 0.7 μm), where some excavated material is redeposited. This area experiences the largest surface displacements, however the sputtered material significantly alters the surface contrast [see Fig. 2(a)] making DIC analysis unreliable there. Since the amplitude of the surface displacements decline rapidly from the hole edge, only the region for which the signal-to-noise ratio is larger than 5 is taken into consideration. Accordingly, the analyzed region is bounded by inner and outer radii $r_1=2.78\ \mu\text{m}$ ($r_0/r_1\cong 0.7$) and $r_2=4.75\ \mu\text{m}$ ($r_0/r_2\cong 0.4$) as shown in Fig. 2(b) where the maximum principal strains in radial directions are mapped. It is evident from the surface displacements [Fig. 2(c), (d)] that the state of in-plane compressive stress (since the displacements tend to close the hole) in the vicinity of the micro-hole is non-uniform and varies harmonically around the hole. The largest compressive stress acts approximately along the sample (x direction). Subsequently we show how these mapped displacements can be converted into stress profiles.

Stress Reconstruction Method

The analytical solution for the stress-strain state of a cylindrical hole in an isotropic material, where the stresses σ_N , σ_T and angle ϕ are the unknowns, was given by Muskhelishvili, who used the potential function of the complex method [38]. Following an argument in [6], the three unknowns (σ_x , σ_y and σ_{xy}) can be determined from equation (1) using three values of the relieved displacements (U_I , U_{II} and U_{III}), each measured between two points, which are determined at the intersection of a circle of radius $r > r_0$ and a line crossing the centre of the hole,

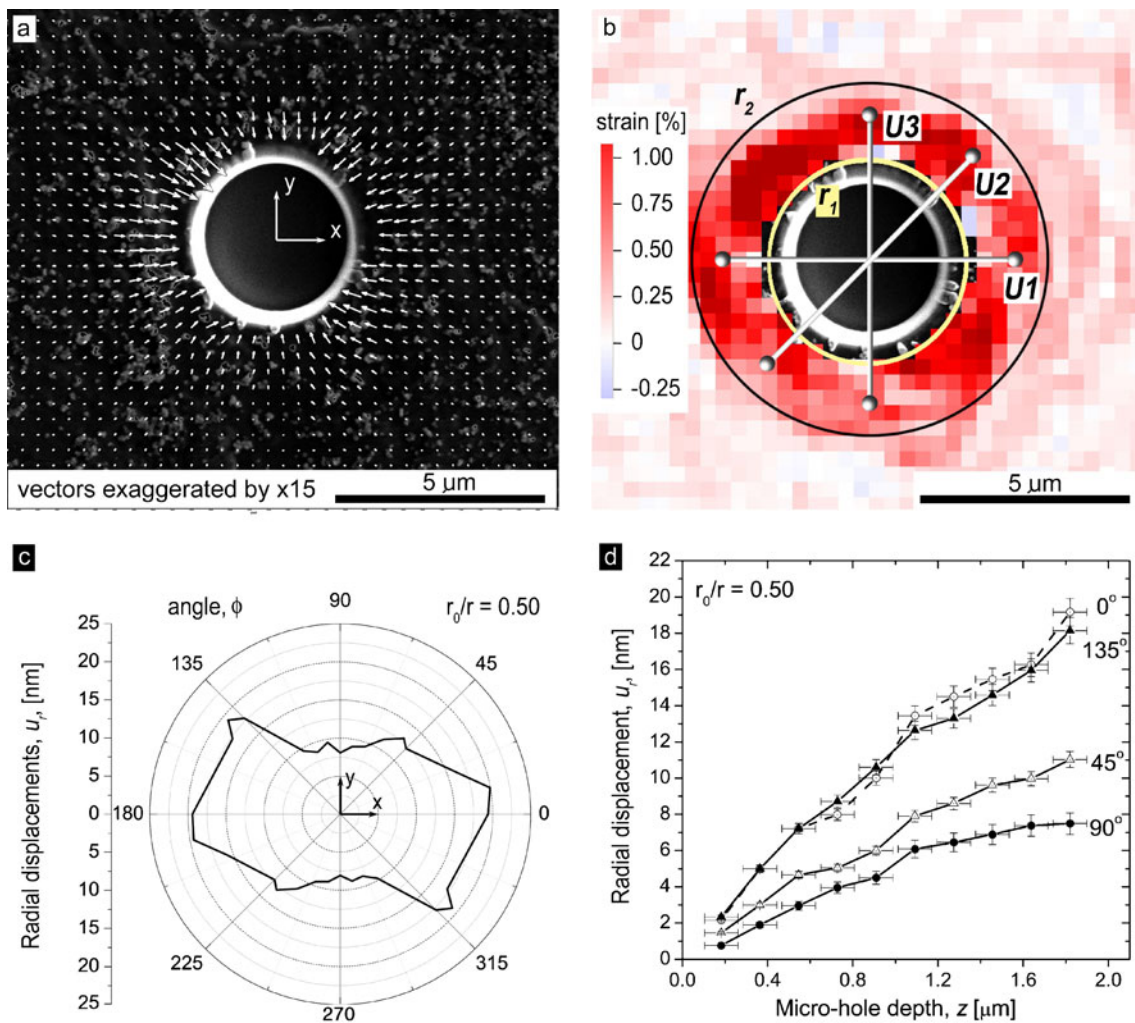


Fig. 2 (colour online) Digital image correlation analysis results for the final increment, $z=1.8\pm 0.07\ \mu\text{m}$: (a) 2-D displacement vector field (vectors are exaggerated by $\times 15$); (b) 2-D map of the maximum principal strains; (c) radial displacements, u_r , vs. angle, ϕ , measured at distance $r_0/r=0.5$; (d) radial displacements, u_r , vs. hole depth, z , measured at distance $r_0/r=0.5$ and angles, $\phi=0^\circ, 45^\circ, 90^\circ$ and 135°

where the three lines are positioned at $\theta=0^\circ, 45^\circ$ and 90° [see Fig. 2(b)].

Digital image correlation data allows us to measure up to several hundred data points, therefore the calculation can be repeated for a number of radial ($r_0/r\cong 0.6, 0.5$ and 0.45) and angular ($0^\circ < \theta + \phi < 180^\circ, \Delta\phi\cong 5^\circ$) positions. Thus relieved displacements can be expressed compactly in matrix form in terms of radial and angular coordinates, as follows

$$\begin{bmatrix} U_I(r, \phi) \\ U_{II}(r, \phi) \\ U_{III}(r, \phi) \end{bmatrix} = \begin{bmatrix} A(r) & B(r) & 0 \\ A(r) & 0 & 2B(r) \\ A(r) & -B(r) & 0 \end{bmatrix} \begin{bmatrix} P \\ Q \\ T \end{bmatrix} \Rightarrow [U(r, \phi)] = [\Theta(r)][\Pi] \quad (1)$$

$$P = \sigma_x(\phi) + \sigma_y(\phi), \quad Q = \sigma_x(\phi) - \sigma_y(\phi), \quad \text{and} \quad (2)$$

$$T = 2\tau_{xy}(\phi)$$

where $U_I \cong 2u_N^{(0^\circ+\phi)}$, $U_{II} \cong 2u_N^{(45^\circ+\phi)}$, $U_{III} \cong 2u_N^{(90^\circ+\phi)}$. Stresses $\sigma_x(\phi)$, $\sigma_y(\phi)$ and $\tau_{xy}(\phi)$ are calculated in local rectangular coordinates rotated ϕ degrees in the anti-clockwise direction (see Fig. 1). Coefficients A and B are the cumulative stress relaxation functions (CRFs) (for equibiaxial and pure shear states of stress) either obtained by FEA,¹ or from an experiment where a micro-hole is ion-milled into material with known residual stresses. Separate finite element calculations are required for the coefficients A and B for various combinations of hole depth and stress location.

A superposition argument [5] allowed us to calculate the calibration coefficients in a linear-elastic-isotropic² material ($E=95\pm\text{GPa}$, and $\nu=0.37$ [39]) directly using loadings where the reference residual stresses, for which

¹ Abaqus 6.8 package was used.

² As a metallic glass the assumption of isotropy at this length-scale is easily justified.

associated deformations have simple trigonometric forms,³ are applied with opposite sign to the curved surface of the micro-hole [6]. The remaining surfaces of the FE models were unstressed. Our FE model was assembled using 8-node (quadratic approximation function) square-shape axisymmetric elements where the size of elements in the vicinity⁴ of the hole was 1/30th the hole diameter, see Fig. 3.

In order to make the coefficients independent of the hole diameter and the elastic constants, it is useful to convert the CRFs into dimensionless cumulative stress relaxation functions (DCRFs);

$$\tilde{A}(r) = \frac{E}{r_0(1 + \nu)}A(r), \quad \tilde{B}(r) = \frac{E}{r_0}B(r) \quad (3)$$

The DCRFs $\tilde{A}(r)$ and $\tilde{B}(r)$ are tabulated in the Appendix for a number of radial locations ($r_0/r \approx 0.6, 0.5$ and 0.45). Fig. 4 shows a graphical representation of the DCRFs for the hole radius $r_0/r = 0.50$. Both functions are well-behaved over the range plotted, indeed no singularities exist over the practical range of hole depths. In practice, the hole depth should be equal or smaller than the hole radius [5]. For larger hole depths the residual stress solution is ill-conditioned, resulting in large uncertainties in the stress estimates. Both functions have a shape similar to those in [5].

In general, each micro-hole-drilling measurement will comprise an irregularly spaced series of hole depth increments. The DCRFs corresponding to these specific hole depths may be determined by interpolating within the set of values found by the finite-element analyses and tabulated in the Appendix most easily by using the bivariate interpolation scheme, as described there. Adjustments for small changes in the hole radius can be made, since the DCRFs for given normalized hole-depth and stress position are very nearly proportional to the square of the hole radius (see details in [5]).

Equations in matrix form (1) are solved simultaneously for the residual stresses. By transforming the measured stresses into the global coordinates:

$$\begin{bmatrix} \hat{\sigma}_x \\ \hat{\sigma}_y \\ \hat{\tau}_{xy} \end{bmatrix} = \begin{bmatrix} \cos^2\phi & \sin^2\phi & -2\sin\phi\cos\phi \\ \sin^2\phi & \cos^2\phi & 2\sin\phi\cos\phi \\ \sin\phi\cos\phi & -\sin\phi\cos\phi & \cos^2\phi - \sin^2\phi \end{bmatrix} \begin{bmatrix} \sigma_x(\phi) \\ \sigma_y(\phi) \\ \tau_{xy}(\phi) \end{bmatrix} \quad (4)$$

we can estimate the three unknown stresses (σ_x, σ_y and τ_{xy}) from the mean stresses ($\bar{\sigma}_x, \bar{\sigma}_y, \bar{\tau}_{xy}$) acting in the directions

x and y (see Fig. 1). We can extend the methodology presented above to reconstruct the residual-stress depth profiles using the Unit Pulse Method [4, 5]. Equation (1) relates the measured displacements, U , to the equivalent uniform in-plane residual stress in the first depth-increment. Generalizing to k depth-increments we obtain

$$\begin{bmatrix} U_I^{(1)} \\ U_{II}^{(1)} \\ U_{III}^{(1)} \\ U_I^{(2)} \\ U_{II}^{(2)} \\ U_{III}^{(2)} \\ \vdots \\ U_I^{(i)} \\ U_{II}^{(i)} \\ U_{III}^{(i)} \end{bmatrix} = \begin{bmatrix} a_{11} & b_{11} & 0 & 0 & 0 & 0 & \cdots & 0 & 0 & 0 \\ a_{11} & 0 & 2b_{11} & 0 & 0 & 0 & \cdots & 0 & 0 & 0 \\ a_{11} & -b_{11} & 0 & 0 & 0 & 0 & \cdots & 0 & 0 & 0 \\ a_{21} & b_{21} & 0 & a_{22} & b_{22} & 0 & \cdots & 0 & 0 & 0 \\ a_{21} & 0 & 2b_{21} & a_{22} & 0 & 2b_{22} & \cdots & 0 & 0 & 0 \\ a_{21} & -b_{21} & 0 & a_{22} & -b_{22} & 0 & \cdots & 0 & 0 & 0 \\ \vdots & \vdots & \vdots & \vdots & \vdots & \vdots & \ddots & \vdots & \vdots & \vdots \\ a_{i1} & b_{i1} & 0 & a_{i2} & b_{i2} & 0 & \cdots & a_{ii} & b_{ii} & 0 \\ a_{i1} & 0 & 2b_{i1} & a_{i2} & 0 & 2b_{i2} & \cdots & a_{ii} & 0 & 2b_{ii} \\ a_{i1} & -b_{i1} & 0 & a_{i2} & -b_{i2} & 0 & \cdots & a_{ii} & -b_{ii} & 0 \end{bmatrix} \begin{bmatrix} P^{(1)} \\ Q^{(1)} \\ T^{(1)} \\ P^{(2)} \\ Q^{(2)} \\ T^{(2)} \\ \vdots \\ P^{(i)} \\ Q^{(i)} \\ T^{(i)} \end{bmatrix} \quad (5)$$

in compact form

$$\begin{bmatrix} U^{(1)} \\ U^{(2)} \\ \vdots \\ U^{(i)} \end{bmatrix} = \begin{bmatrix} \Theta_{11} & 0 & 0 & 0 \\ \Theta_{21} & \Theta_{22} & 0 & 0 \\ \vdots & \vdots & \ddots & 0 \\ \Theta_{i1} & \Theta_{i2} & \cdots & \Theta_{ii} \end{bmatrix} \begin{bmatrix} \Pi^{(1)} \\ \Pi^{(2)} \\ \vdots \\ \Pi^{(i)} \end{bmatrix} \Leftrightarrow \hat{U}^{(i)} = \hat{\Theta}_{ij}^{(i)} \hat{\Pi}^{(i)} \quad (6)$$

where, to be concise we omitted the r, ϕ dependencies, e.g. $U^{(i)}$ represents $U^{(i)}(r, \phi)$. $U^{(i)}$ is a vector of the displacements measured by DIC when the hole-depth is h_k ; $\Pi^{(i)}$ is a vector of the uniform stress terms $P^{(i)}, Q^{(i)}, T^{(i)}$ acting in stress layer ΔH_j , lying between depths H_{j-1} and H_j ; and $\Theta(h_i, \Delta H_j)$ is a matrix of the incremental calibration functions (ICFs) relating the relieved displacements to the uniform stress terms acting at depth H_j when the hole depth equals h_i . Following arguments in [5] and if we know the CRFs obtained from FEA, the ICFs can be determined easily for any number and size of hole-depth increments by simple subtractions. We can obtain the desired solution of the stress variation with depth by inverting equation (6). We obtained a tentative solution (the linear operator equations) to equation (6) using pseudo-inversion. The three unknown stresses (σ_x, σ_y and τ_{xy}) for each hole-increment can then be estimated by the mean stresses ($\bar{\sigma}_x, \bar{\sigma}_y$ and $\bar{\tau}_{xy}$) acting in the directions x and y using similar relationships to equations (2) and (4).

Regularisation

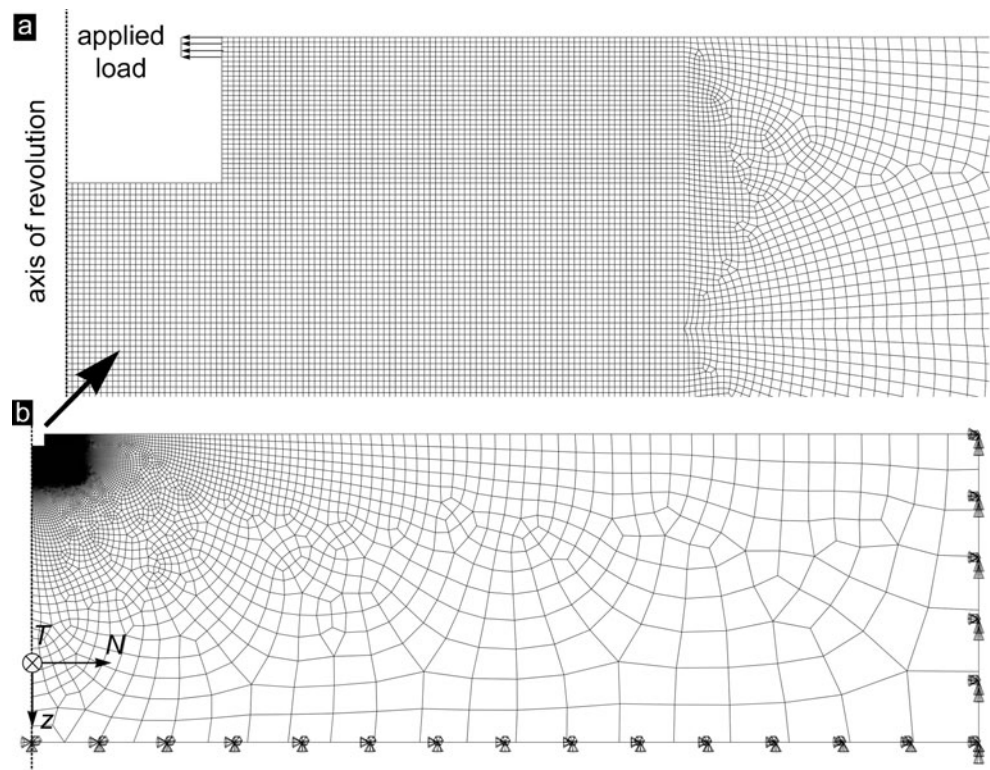
In practice measured data are a convolution of measurement noise and the ‘true’ values. The pseudo-inversion algorithm yields stable residual stress solutions if the coefficients of

³ Asymmetric zeroth-harmonic radial displacement (for coefficient \tilde{A}) and symmetric second-harmonic radial and circumferential displacement (for coefficient \tilde{B}).

⁴ The vicinity of the hole is equal $6 \times$ the hole diameter in radial and hole depth directions.



Fig. 3 Axisymmetric FE model for a hole of depth equal to the hole radius. **(a)** meshing details in the vicinity of a hole, **(b)** meshed FE model



the ICFs matrix are of the same order of magnitude. However, the incremental micron-hole milling processes expressed in mathematical terms using pulse functions produces relatively small matrix entries in the diagonal bands of the ICFs matrix. Thus, the linear operator equations for a large number of increments become numerically ill-conditioned leading to unstable solutions, giving large oscillations of the residual stress solution with depth. These problems can be suppressed by careful selection of the hole-depths at which the residual stresses are calculated, which usually lead to in-depth stress profiles inferred using a reduced number of data points [40, 41].

Alternatively in order to overcome the numerical ill-conditioning, the linear operator equations can be mathematically modified to stabilize the residual stress solution and to reduce the amplification of noise. These equations are usually modified using variants of the well-known Tikhonov regularization method [32, 42–45]. This method states the problem of minimizing the square of the Euclidean norm of the residuals of the residual stress solution according to chosen strategy (*a priori* or *a posteriori*) of selecting the regularization parameter, α . Since *a priori* methods require the definition of an additional unknown smoothness parameter, ν , [43] we used an *a posteriori* selection criteria following [33]. Within the adopted regularization scheme we select the regularization parameter, α , based on an estimate $\delta_{est}(r)$ of the measurement noise in the measured data $\tilde{U}^{(i)}$. The parameter α was

chosen in such way that the Euclidean norm of regularized solution discrepancy is equal the discrepancy level in the measured data, δ , in our case the discrepancy in displacement measurement. Since the displacements are mapped at several radial positions ($\hat{\Theta}_{ij}^{(i)}(r), r_0/r=0.6, 0.5$ and 0.45), thus the following procedure is repeated for each radial position:

- (i) Estimate the error norm $\delta_{est}(r)$ of the measured displacement vector $\bar{U}^{(i)}(r)$, which is given by $\delta_{est}(r) = \left\| \tilde{U}_{rnd}^{(i)} + \tilde{U}_{sys}^{(i)}(r) \right\|$. Here, $\tilde{U}_{rnd}^{(i)}$ is the random error vector obtained by replacing each element in $\bar{U}^{(i)}(r)$ by appropriate random error value from Table 1, and $\tilde{U}_{sys}^{(i)}$ is the systematic error vector obtained by taking the appropriate percentage value from Table 1 of each element in $\bar{U}^{(i)}(r)$. The elements of vector $\bar{U}^{(i)}(r)$ are calculated as follows using an average value of four angular positions $\phi=0, 45, 90$ and 135° . The random error is calculated as the standard deviation of DIC displacement of the evaluated sets of 1015 x and y displacements. Whereas the systematic error is the scatter in displacement measurement using different patch sizes and different patch overlap (OV): 32×32 pixels OV by 25%, 64×64 pixels OV by 25%, 64×64 pixels OV by 50%, 64×64 pixels OV by 75%; which in this case is $\pm 4\%$ of the measured value.
- (ii) Calculate the least-squares solution discrepancy δ_0 for the non-bounded problem for each radial position using $\delta_0(r) = \left\| \hat{\Theta}_{ij}^{(i)} \hat{\Pi}^{(i)} - \tilde{U}^{(i)} \right\|$.

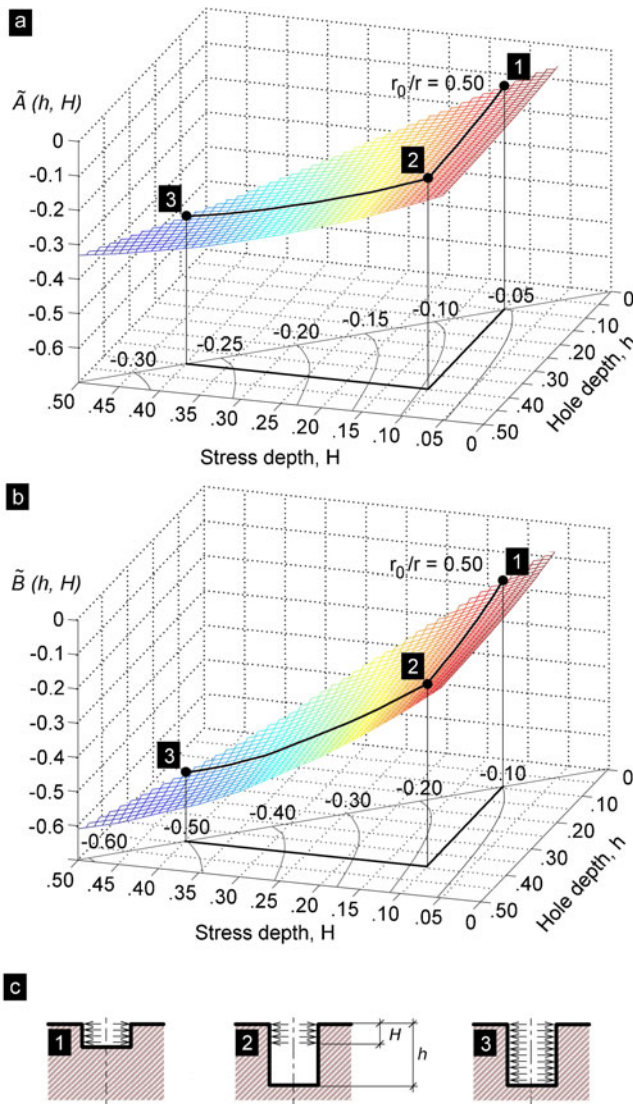


Fig. 4 (colour online) Graphical representation of the dimensionless cumulative stress relaxation functions for the hole radius $r_0/r=0.50$: (a) $\hat{A}(h, H)$ and (b) $\hat{B}(h, H)$; (c) shows the corresponding hole depth, h , and stress depth, H

(iii) Solve for the regularized solution $\hat{\Pi}_\alpha^{(i)}$. Iterate by varying the regularization parameter α using a bisection algorithm, until $\|\hat{\Theta}_{ij}^{(i)} \hat{\Pi}_\alpha^{(k)} - \hat{U}^{(i)}\| = \delta(r)$. The discrepancy in displacement measurement after regularization, $\delta(r)$, is determined from equation (7) following from [33], thus

$$\delta(r) = \begin{cases} \delta_0(r) + 0.25\delta_0(r) \exp(\Delta\delta(r)/0.25\delta_0(r)), & \Delta\delta(r) \leq 0 \\ \delta_{est}(r) + 0.25\delta_0(r), & \Delta\delta(r) > 0 \end{cases} \text{ where} \quad \Delta\delta(r) = \delta_{est}(r) - \delta_0(r) \quad (7)$$

Table 1 Estimated DIC analysis accuracy

Component	Random error	Systematic error
u_N	0.36 nm (0.0147 pixel)	±4% of measured value

The discrepancy in the measured displacements, the least-squares solution discrepancy and the discrepancy in displacement measurement after regularization for different radial locations ($r_0/r=0.6, 0.5$ and 0.45), for 10 and 5 depth increments are shown in Table 2.

Uncertainty in Stress Determination

For the $\Gamma\mu$ HD method, uncertainties have five main sources:

- (a) displacement measurement errors, which include DIC calculation errors, material redeposition and additional residual stresses induced by Ga^+ ions implantation;
- (b) hole depth measurement errors, which include non-flatness of the bottom of the hole;
- (c) hole diameter measurement errors, which include tapering of the hole and deviation from roundness;
- (d) incorrect material constants;
- (e) hole eccentricity, which includes possible focused ion beam drifts.

Note that the sources of type (a) are independent of the stresses that are present. Whereas the sources of uncertainties (b)–(e) are proportional to the residual stresses and affect the ICFs matrix, $\hat{\Theta}_{ij}^{(i)}$. In this study, following the argument in [40], we include only the sources (a) where the strain perturbations, e.g. $[\delta U^{(i)}]$ (the random error and the systematic error) result in calculated residual stress perturbation, e.g. $[\delta \Pi_\alpha^{(i)}]$. Thus, the mean standard deviation (for $r_0/r=0.6, 0.5$ and 0.45) in the uncertainty of inferred stress is calculated from following equation

$$SD \hat{\Pi}^{(i)} = \sqrt{\sum_j \left(\left[\left(\hat{\Theta}_{ij}^{(i)} \right)^T \hat{\Theta}_{ij}^{(i)} \right]^{-1} \left(\hat{\Theta}_{ij}^{(i)} \right)^T \delta U^{(i)} \right)^2} \quad (8)$$

The standard deviation for regularized stresses, $SD \hat{\Pi}_\alpha^{(i)}$, is calculated similarly. In this study the stress calculation uncertainty is quoted as ±1.64 standard deviations (90% probability bounds). Equation (8) quantifies the propagation of uncertainties with the distance from the surface. Physically, following the St. Venant’s principle, it demon-

Table 2 The discrepancy of the measurement for different radial locations and depth increments

	δ_{est} [nm]			δ_0 [nm]			δ [nm]		
r_0/r	0.6	0.5	0.45	0.6	0.5	0.45	0.6	0.5	0.45
10 ^a	2.38	1.64	1.09	1.62	0.64	0.41	2.78	1.8	1.19
5 ^a	1.05	0.55	0.40	0.43	0.10	0.22	1.16	0.48	0.23

^a number of increments



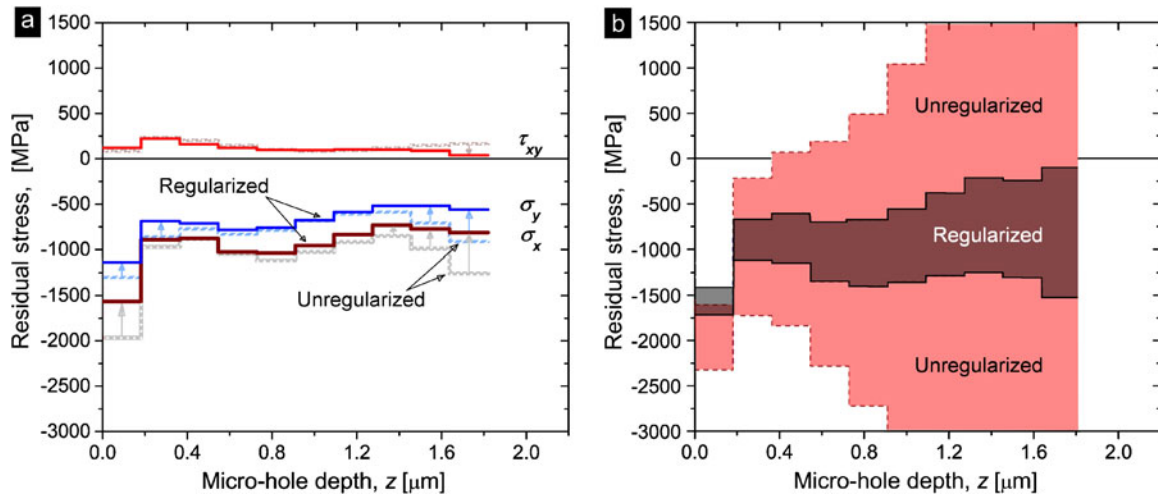


Fig. 5 (colour online) Inferred in-plane residual stresses profiles (σ_x , σ_y and τ_{xy}) as a function of depth from the deformed surface for a depth resolution (increment) of 180 nm. In (a) the solid lines indicate for the regularised solutions and the dashed lines the unregularised ones, in (b) the 90% probability bounds for σ_x are indicated (black–regularised and red–unregularised)

strates diminishing efficiency of hole drilling based stress estimation methods to evaluate stresses deep below the surface.

It was shown previously that the UPM can reconstruct highly non-uniform stresses [4, 5]. However, the estimates do not adequately fit the original stress profiles (giving step-shaped inferred stress profiles), thus an additional source of error potentially exists, namely ‘the unit pulse model uncertainty’. Generally, the unit pulse model error is disproportionate to the number of hole-depth increments. Indeed a similar concept of ‘model error’ was introduced by Prime & Hill [46] for the series expansion method. It was shown that the uncertainties of measured data and the model uncertainties are two major sources of uncertainties of the stress calculations [46].

Results

Figure 5(a) shows the back-calculated unregularized and regularised in-plane residual stress components as a function of depth from the deformed surface using a depth increment (resolution) of 180 nm. The corresponding estimates for a depth resolution of 360 nm are shown in Fig. 6(a). In each case the 90% uncertainty bounds are shown for σ_x only (those for other stress components are of the same order of magnitude and are thus omitted in the figures for the sake of clarity). It is clear from Figs. 5 and 6 that the difference between the best estimates of the stress profiles is relatively small between the regularised and unregularised schemes, but that there is a much larger variation between the uncertainty bounds. For the unreg-

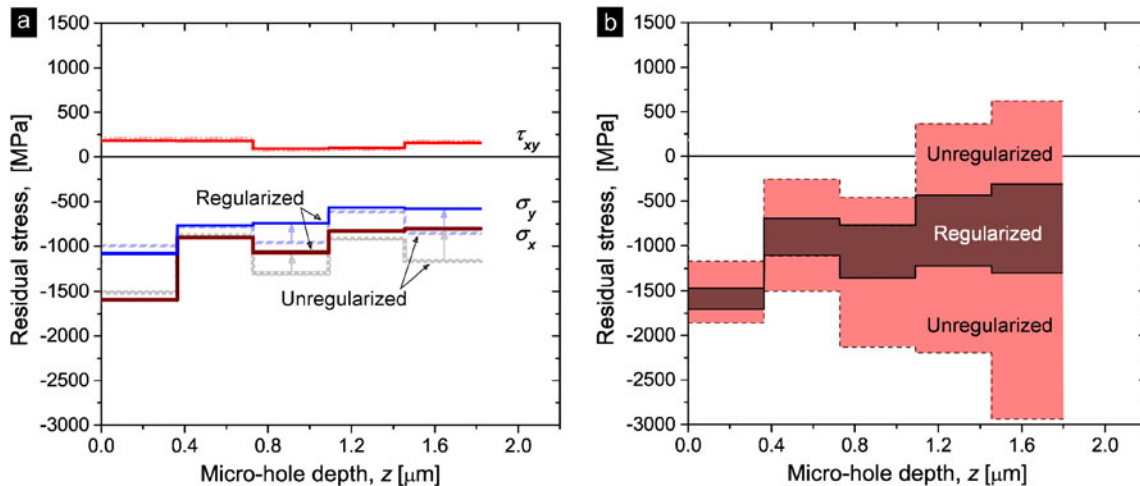


Fig. 6 (colour online) Inferred in-plane residual stresses profiles (σ_x , σ_y and τ_{xy}) as a function of depth from the deformed surface for a depth resolution (increment) of 360 nm where τ_{xy} is larger about 30 MPa for unregularized results. In (a) the solid lines indicate for the regularised solutions and the dashed lines the unregularised ones, in (b) the 90% probability bounds for σ_x are indicated (black–regularised and red–unregularised)

ularised case, except for the first increment the bounds become unacceptably wide.

The compressive residual stress component σ_x in the longitudinal direction of the sample appears to be some 30% higher than the stress component σ_y in the transverse direction. There is some evidence of shear stresses (~120 MPa) such that the principal stresses lie at around 15° to the specimen length.

The recorded longitudinal stress (σ_x) average to a value around $-800 \text{ MPa} \pm 90 \text{ MPa}$ (90% bounds) over the evaluation depth (1.8 μm) and compares to $-650 \text{ MPa} \pm 50 \text{ MPa}$ (90% bounds) measured along the sample (x -direction) over a depth of 4.1 μm obtained using a FIB microslotting method [20], and to $920 \text{ MPa} \pm 230 \text{ MPa}$ (90% bounds) in [21] obtained by the down-scaled rosette method averaged over a depth of 2 μm .

Discussion

As expected, unregularized schemes yield unstable (oscillating) solutions with the uncertainty bounds becoming increasingly wider with increasing depth (Figs. 5 and 6). Note that contrary to other work [40], the uncertainty propagation analyses considers the more severe case where

the displacement measurement errors are not all equal. Therefore, the bounds widen sharply especially for the unregularised case with depth and the smaller increments. Mathematically, this behavior reflects the distribution of the coefficients in the matrix ICFs, where the diagonal entries are of an order of magnitude smaller than others. Since our method calculates the average values of the stress components the oscillations in results are not pronounced for larger numbers of depth increments (Fig. 5). On the contrary, the down-scaled rosette method in [21] for the unregularized scheme gives high amplitude oscillations in the estimates for the same number of depth increments. Furthermore, the bounds are more than 3 times further apart than for the current studies.

By reducing of the depth resolution from 180 nm to 360 nm we obtained more accurate results, since the entries in the ICFs matrix are computationally less troublesome and the propagated errors are much smaller [Fig. 6(b) vs. Fig. 5(b)]. In other words, a lower depth resolution yields less uncertainty in the residual stress estimates.

With a regularized scheme, the oscillations in stress estimates and the uncertainty bounds became much closer together (more than 2.5 times smaller than the unregularized stress estimates) being of the same order of magnitude for all depth increments. Mathematically, the regularization

Table 3 The dimensionless cumulative stress relaxation functions $\tilde{A}(h, H)$ for different radial locations

h \ H	0.05	0.10	0.15	0.20	0.25	0.30	0.35	0.40	0.45	0.50
0.05	-0.0145									
0.10	-0.0188	-0.0344								
0.15	-0.0219	-0.0407	-0.0583							
0.20	-0.0244	-0.0457	-0.0664	-0.0847						
0.25	-0.0264	-0.0497	-0.0728	-0.0939	-0.1098					
0.30	-0.0280	-0.0529	-0.0777	-0.1010	-0.1195	-0.1364				
0.35	-0.0293	-0.0553	-0.0816	-0.1064	-0.1268	-0.1463	-0.1617			
0.40	-0.0303	-0.0573	-0.0847	-0.1107	-0.1324	-0.1536	-0.1714	-0.1868		
0.45	-0.0312	-0.0590	-0.0873	-0.1142	-0.1368	-0.1593	-0.1785	-0.1964	-0.2092	
0.50	-0.0321	-0.0607	-0.0897	-0.1174	-0.1409	-0.1643	-0.1846	-0.2028	-0.2202	-0.2362

$\tilde{A}(h, H)$ for $r_d/r = 0.45$

h \ H	0.05	0.10	0.15	0.20	0.25	0.30	0.35	0.40	0.45	0.50
0.05	-0.0215									
0.10	-0.0278	-0.0528								
0.15	-0.0329	-0.0633	-0.0900							
0.20	-0.0370	-0.0716	-0.1031	-0.1273						
0.25	-0.0403	-0.0781	-0.1132	-0.1417	-0.1662					
0.30	-0.0429	-0.0832	-0.1210	-0.1526	-0.1811	-0.2031				
0.35	-0.0449	-0.0871	-0.1269	-0.1606	-0.1920	-0.2177	-0.2399			
0.40	-0.0466	-0.0902	-0.1314	-0.1667	-0.2000	-0.2284	-0.2537	-0.2726		
0.45	-0.0480	-0.0929	-0.1352	-0.1715	-0.2063	-0.2363	-0.2634	-0.2856	-0.3009	
0.50	-0.0494	-0.0953	-0.1387	-0.1760	-0.2119	-0.2427	-0.2717	-0.2938	-0.3155	-0.3324

$\tilde{A}(h, H)$ for $r_d/r = 0.50$

h \ H	0.05	0.10	0.15	0.20	0.25	0.30	0.35	0.40	0.45	0.50
0.05	-0.0337									
0.10	-0.0430	-0.0809								
0.15	-0.0509	-0.0972	-0.1367							
0.20	-0.0571	-0.1097	-0.1563	-0.1904						
0.25	-0.0617	-0.1191	-0.1710	-0.2113	-0.2428					
0.30	-0.0651	-0.1260	-0.1816	-0.2265	-0.2634	-0.2906				
0.35	-0.0677	-0.1311	-0.1892	-0.2373	-0.2777	-0.3097	-0.3335			
0.40	-0.0695	-0.1348	-0.1948	-0.2450	-0.2878	-0.3228	-0.3507	-0.3706		
0.45	-0.0710	-0.1379	-0.1993	-0.2511	-0.2955	-0.3322	-0.3625	-0.3861	-0.4025	
0.50	-0.0724	-0.1409	-0.2037	-0.2570	-0.3025	-0.3402	-0.3723	-0.3953	-0.4195	-0.4338

$\tilde{A}(h, H)$ for $r_d/r = 0.60$



Table 4 The dimensionless cumulative stress relaxation functions $\tilde{B}(h, H)$ for different radial locations

h \ H	0.05	0.10	0.15	0.20	0.25	0.30	0.35	0.40	0.45	0.50
0.05	-0.0266									
0.10	-0.0345	-0.0650								
0.15	-0.0402	-0.0768	-0.1080							
0.20	-0.0448	-0.0862	-0.1231	-0.1529						
0.25	-0.0485	-0.0937	-0.1351	-0.1700	-0.2026					
0.30	-0.0514	-0.0997	-0.1444	-0.1833	-0.2207	-0.2493				
0.35	-0.0537	-0.1044	-0.1518	-0.1935	-0.2343	-0.2676	-0.3009			
0.40	-0.0556	-0.1082	-0.1577	-0.2015	-0.2446	-0.2813	-0.3188	-0.3460		
0.45	-0.0572	-0.1115	-0.1627	-0.2082	-0.2530	-0.2919	-0.3320	-0.3635	-0.3859	
0.50	-0.0588	-0.1146	-0.1674	-0.2143	-0.2605	-0.3010	-0.3432	-0.3753	-0.4061	-0.4388

$\tilde{B}(h, H)$ for $r_d/r = 0.45$

h \ H	0.05	0.10	0.15	0.20	0.25	0.30	0.35	0.40	0.45	0.50
0.05	-0.0424									
0.10	-0.0538	-0.1000								
0.15	-0.0630	-0.1192	-0.1670							
0.20	-0.0703	-0.1345	-0.1911	-0.2370						
0.25	-0.0761	-0.1464	-0.2097	-0.2639	-0.3065					
0.30	-0.0805	-0.1557	-0.2240	-0.2842	-0.3341	-0.3805				
0.35	-0.0839	-0.1628	-0.2348	-0.2994	-0.3541	-0.4074	-0.4438			
0.40	-0.0866	-0.1684	-0.2432	-0.3110	-0.3688	-0.4272	-0.4694	-0.5026		
0.45	-0.0888	-0.1731	-0.2501	-0.3203	-0.3803	-0.4418	-0.4873	-0.5264	-0.5550	
0.50	-0.0908	-0.1775	-0.2565	-0.3289	-0.3907	-0.4536	-0.5029	-0.5415	-0.5819	-0.6110

$\tilde{B}(h, H)$ for $r_d/r = 0.50$

h \ H	0.05	0.10	0.15	0.20	0.25	0.30	0.35	0.40	0.45	0.50
0.05	-0.0337									
0.10	-0.0430	-0.0809								
0.15	-0.0509	-0.0972	-0.1367							
0.20	-0.0571	-0.1097	-0.1563	-0.1904						
0.25	-0.0617	-0.1191	-0.1710	-0.2113	-0.2428					
0.30	-0.0651	-0.1260	-0.1816	-0.2265	-0.2634	-0.2906				
0.35	-0.0677	-0.1311	-0.1892	-0.2373	-0.2777	-0.3097	-0.3335			
0.40	-0.0695	-0.1348	-0.1948	-0.2450	-0.2878	-0.3228	-0.3507	-0.3706		
0.45	-0.0710	-0.1379	-0.1993	-0.2511	-0.2955	-0.3322	-0.3625	-0.3861	-0.4025	
0.50	-0.0724	-0.1409	-0.2037	-0.2570	-0.3025	-0.3402	-0.3723	-0.3953	-0.4195	-0.4338

$\tilde{B}(h, H)$ for $r_d/r = 0.60$

methodology redistributes the entries in the augmented ICFs matrix making them of the same order of magnitude along the diagonal. Thus, the residual stress estimates and uncertainty bounds for the depth resolution of 180 nm and 360 nm are comparable. Therefore ‘the unit pulse model uncertainty’ is reduced. The error propagation analysis for the regularized algorithm of the down-scaled rosette method [21] yielded bounds about 3 times larger than the bounds estimated herein. The down-scaled rosette method tends to overestimate the stress estimates by about 15%.

The error analysis for the results estimated from a single depth increment at depth of 1.8 μm yields narrow uncertainty bounds of ±75 MPa. In this case, the incremental micro-hole-drilling method loses its capability of inferring depth profiles of stresses and ‘the unit pulse model uncertainty’ will reach its maximum. Qualitatively, from the current study, we can say that ‘the unit pulse model uncertainty’ is disproportionate to the depth resolution and is coupled with unregularized and regularized probability bounds of residual stress estimates.

The uncertainties in the displacement measurements are relatively large (particularly the systematic error), which result in widely spaced uncertainty bounds, even for regularized analysis. Therefore, to achieve consistent and reliable SEM measurements for use with DIC (to reduce the

source of errors included in the point (a) in Section 3.), the surface must be characterized by a dense, random, high-contrast surface speckle pattern, as discussed and analyzed in [30]. Ideally, the random error of displacement mapping should be reduced to below 0.005 pixels and the systematic error should not exceed about 1.5%.

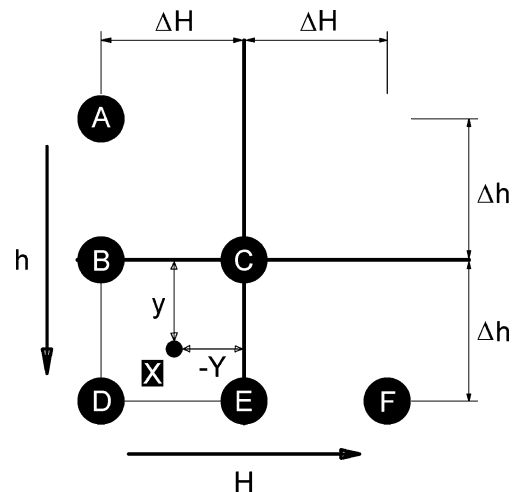


Fig. 7 Triangular scheme for interpolating the tabulated values of $\tilde{A}(h, H)$ and $\tilde{B}(h, H)$

Conclusions

In summary, this work presents a new method for mapping in-plane residual or applied stresses incrementally as a function of depth at the micron-scale laterally and sub-micron scale depth-wise. The proposed methodology reconstructs the residual stress distribution from full-field radial displacements. The results obtained agree within the uncertainties with the residual stresses inferred using the down-scaled rosette method ($-920 \text{ MPa} \pm 230 \text{ MPa}$ (90% bounds)) averaged over $2 \text{ }\mu\text{m}$ depth in [21] and that obtained using a FIB microslotting method ($-650 \text{ MPa} \pm 50 \text{ MPa}$ (90% bounds)) for the x-direction [20] averaged over a depth of $4.1 \text{ }\mu\text{m}$. In addition the method indicated that the principal axes were oriented at 15° to the long axis of the bar. By mapping the radial displacement full-field we reduced the separation of the bounds by about 3 times compared with the down-scaled rosette method. The stabilization approach based on the Tikhonov regularization efficiently reduced the oscillations in stress estimates and substantially narrowed the bounds of stress estimates (more than 2.5 times). In addition, the regularization allowed us to increase the depth resolution from 360 nm to 180 nm without a significant increase of residual stress estimations uncertainty.

The results of the current work and surface decoration methods developed in [30] point to the scalability of this method to map residual stresses in volumes as small as $1 \times 1 \times 0.2 \text{ }\mu\text{m}^3$ or less. The potential applications of this technique are wide ranging, including stresses in amorphous thin films, MEMS components and devices, organic electronic devices, nanostructured materials, etc. Though applicable to crystalline materials, for amorphous materials our micro-hole milling method has few competitors.

Acknowledgments The measurements were made within the Stress and Damage Characterization Unit at the University of Manchester, U.K., supported by the Light Alloys Towards Environmentally Sustainable Transport (LATEST) EPSRC Portfolio Project. We are grateful to P. Liaw (the University of Tennessee, U.S.A.) and Y. Yokoyama (Himeji Institute of Technology, Japan) for provision of the sample; to P. Xiao (the University of Manchester, U.K.) for YSZ nano powder and A. Gholinia (the University of Manchester, U.K.) for technical and scientific suggestions during the experiment and G.S. Schajer for advice.

Appendix

Bivariate interpolation of tabulated dimensionless cumulative stress relaxation functions [5]

The dimensionless cumulative stress relaxation functions (DCRFs) are summarised in Tables 3 and 4.

The Fig. 7 illustrates the scheme for bivariate interpolation of the tabulated DCRFs $\tilde{A}(h, H)$ and $\tilde{B}(h, H)$. Point, X ,

represents the desired (h, H) coordinates, and points, $A-F$, represent the (h, H) coordinates of a triangular group of six values from Tables 3 or 4.

Dimensionless coordinates (Y, y) relate the (h, H) coordinates of points, X , to those of the central point, C , as follows

$$H_X = H_C + Y \Delta H, \quad h_X = h_C + y \Delta h \quad (\text{A1})$$

where $\Delta H = \Delta h = 0.05$. Within the area $BCDE$ of Fig. 7, $-1 \leq Y \leq 0$, and $-1 \leq y \leq 0$. For the best interpolation accuracy, points, $A-F$, should be chosen from Tables 3 and 4 such that point, X , falls within, or as close as possible, to area $BCDE$. Using a quadratic interpolation polynomial, the estimated value at point, X , is

$$\begin{aligned} f_x = & y(y-1)/2f_A + (1-y)(y-Y)f_B + (1-y) \\ & \times (1+Y)f_C + (y-Y)(y-Y-1)/2f_D \\ & + (1+Y)(y-Y)f_E + Y(1+Y)/2f_F \end{aligned} \quad (\text{A2})$$

where f_X, f_A, f_B , etc. are the $\tilde{A}(h, H)$ or $\tilde{B}(h, H)$ values at points X, A, B , etc.

References

- Withers PJ (2007) Residual stress and its role in failure. Rep Prog Phys 70(12):2211–2264. doi:10.1088/0034-4885/70/12/R04
- Schajer GS, Prime MB (2007) Residual stress solution extrapolation for the slitting method using equilibrium constraints. ASME J Eng Mater Technol 129(2):227–232. doi:10.1115/1.2400281
- Schajer GS, An Y (2010) Residual stress determination using cross-slitting and dual-axis ESPI. Exp Mech 50:169–177. doi:10.1007/s11340-009-9317-7
- Schajer GS (1988) Measurement of non-uniform residual-stresses using the hole-drilling method. 1. Stress calculation procedures. ASME J Eng Mater Technol 110(4):338–343
- Schajer GS (1988) Measurement of non-uniform residual-stresses using the hole-drilling method. 2. Practical application of the integral method. ASME J Eng Mater Technol 110(4):344–349
- McGinnis MJ, Pessiki S, Turker H (2005) Application of three-dimensional digital image correlation to the core-drilling method. Exp Mech 45(4):359–367. doi:10.1177/0014485105055435
- Cárdenas-García JF, Preidikman S (2006) Solution of the moire' hole drilling method using a finite-element-method-based approach. Int J Solids Struct 46:6751–6766. doi:10.1016/j.ijsolstr.2006.02.010
- Beghini M, Bertini L, Mori LF, Rosellini W (2009) Genetic algorithm optimization of the hole-drilling method for non-uniform residual stress fields. J Strain Anal 44:105–115. doi:10.1243/03093247JSA457
- Schajer GS, Stainzig M (2010) Dual-axis hole-drilling ESPI residual stress measurements. ASME J Eng Mater Technol 132:011007_1-5. doi:10.1115/1.3184035.
- Flaman MT, Herring JA (1982) Comparison of four hole-producing techniques for the center-hole residual-stress measurement method. Exp Tech 9(8):30–32
- Vangi D (1994) Data managements for the evaluation of residual-stresses by the incremental hole-drilling method. ASME J Eng Mater Technol 116(4):561–566

12. Klein CA (2000) How accurate are Stoney's equation and recent modifications. *J Appl Phys* 88(9):5487–5489
13. Sabate N, Vogel D, Gollhardt A, Keller J, Cane C, Gracia I, Morante JR, Michel B (2006) Measurement of residual stress by slot milling with focused ion-beam equipment. *J Micromechanics Microengineering* 16(2):254–259. doi:10.1088/0960-1317/16/2/009
14. Kang KJ, Yao N, He MY, Evans AG (2003) A method for in situ measurement of the residual stress in thin films by using the focused ion beam. *Thin Solid Films* 443:71–77. doi:10.1016/S0040-6090(03)00946-5
15. McCarthy J, Pei Z, Becker M, Atteridge D (2000) FIB micro-machined submicron thickness cantilevers for the study of thin film properties. *Thin Solid Films* 358(1–2):146–151
16. Massl S, Keckes J, Pippin R (2008) A new cantilever technique reveals spatial distributions of residual stresses in near-surface structures. *Scr Mater* 59(5):503–506. doi:10.1016/j.scriptamat.2008.04.037
17. Vogel D, Sabate N, Gollhardt A, Keller J, Auersperg J, Michel, B (2006) FIB based measurement of local residual stresses on microsystems. in *Proceedings of SPIE - The International Society for Optical Engineering* San Diego, CA. 2006. 6175: 617505. doi:10.1117/12.658298
18. Korsunsky AM, Sebastiani M, Bemporad E (2010) Residual stress evaluation at the micrometer scale: analysis of thin coatings by FIB milling and digital image correlation. *Surf Coat Technol* 205:2393–2403. doi:10.1016/j.surfcoat.2010.09.033
19. Cho S, Cárdenas-García JF, Chasiotis I (2005) Measurement of nanodisplacements and elastic properties of MEMS via the microscopic hole method. *Sens and Actuators A* 120:163–171. doi:10.1016/j.sna.2004.11.028
20. Winiarski B, Langford LR, Tian J, Yokoyama Y, Liaw PK, Withers PJ (2010) Mapping residual-stress distributions at the micron scale in amorphous materials. *Metall Mater Trans A* 41A:1743–1751. doi:10.1007/s11661-009-0127-4
21. Winiarski B, Withers PJ (2010) Mapping residual stress profiles at the micron scale using FIB micro-hole drilling. *Appl Mech Mater* 24–25:267–272. doi:10.4028/www.scientific.net/AMM.24-25.267
22. Winiarski B, Wang G, Xie X, Cao Y, Shin Y, Liaw PK and Withers PJ (2011) Mapping Residual-Stress Distributions in a Laser-Peened Vit-105 Bulk-Metallic Glass Using the Focused-Ion-Beam Micro-Slotting Method, *Proceedings of MRS Fall Meeting, 29 November - 3 December 2010, Boston, MA, U.S.A.*
23. Liaw PK, Xie X, Cao Y, Winiarski B, Wang G, Withers PJ, Shin Y (2011) Surface Modification of Bulk-Metallic Glasses by Laser-Peening Process *Proceedings of 2011 NSF Engineering Research and Innovation Conference, January 4–7 2011, Atlanta, GA, U.S.A.*
24. Cao Y, Xie X, Winiarski B, Wang G, Shin YC, Withers PJ, Liaw PK (2011) Residual Stresses Induced by Laser Shock Peening on Zr-based Bulk Metallic Glass and Its Effect on Plasticity, *Proceedings of TMS2011 Annual Meeting and Exhibition, Bulk Metallic Glasses VIII, Feb. 27 – Mar. 3, 2011 San Diego, California, U.S.A.*
25. Massl S, Keckes J, Pippin R (2007) A direct method of determining complex depth profiles of residual stresses in thin films on a nanoscale. *Acta Mater* 55(14):4835–4844. doi:10.1016/j.actamat.2007.05.002
26. Quinta De Fonseca J, Mummery PM, Withers PJ (2004) Full-field strain mapping by optical correlation of micrographs acquired during deformation. *J Microsc* 218:9–21. doi:10.1111/j.1365-2818.2005.01461
27. Peters WH, Ranson WF (1982) Digital imaging techniques in experimental stress-analysis. *Opt Eng* 21(3):427–431
28. Lecompte D, Smits A, Sven B, Sol H, Vantomme J, Van Hemelrijck D, Habraken AM (2006) Quality assessment of speckle patterns for digital image correlation. *Opt Lasers Eng* 44 (11):1132–1145. doi:10.1016/j.optlaseng.2005.10.004
29. van Kouwen L, Botman A, Hagen CW (2009) Focused electron-beam-induced deposition of 3 nm dots in a scanning electron microscope. *Nano Lett* 9(5):2149–2152. doi:10.1021/nl900717r
30. Winiarski B, Schajer GS, Withers PJ, Surface decoration for improving the accuracy of displacement measurements by Digital Image Correlation in Scanning Electron Microscopy. In Peer-review - *Experimental Mechanics*.
31. Vogel D, Lieske D, Gollhardt A, Keller J, Sabate N, Morante JR, Michel B (2005) FIB based measurements for material characterization on MEMS structures. in *Proceedings of SPIE - The International Society for Optical Engineering, San Diego, CA, 2005.* doi:10.1117/12.599891.
32. Tikhonov AN, Arsenin VY (1977) *Solution of Ill-posed problems.* John Wiley & Sons, New York
33. Tjhung T, Li KY (2003) Measurement of in-plane residual stresses varying with depth by the Interferometric Strain/Slope Rosette and incremental hole-drilling. *ASME J Eng Mater Technol* 125 (2):153–162. doi:10.1115/1.1555654
34. Tian JW, Shaw LL, Wang YD, Yokoyama Y, Liaw PK (2009) A study of the surface severe plastic deformation behaviour of a Zr-based bulk metallic glass (BMG). *Intermetallics* 17(11):951–957. doi:10.1016/j.intermet.2009.04.010
35. Yaofeng S, Pang JHL (2007) Study of optimal subset size in digital image correlation of speckle pattern images. *Opt Lasers Eng* 45(9):967–974. doi:10.1016/j.optlaseng.2007.01.012
36. Jin H, Lu WY, Korellis J (2008) Micro-scale deformation measurement using the digital image correlation technique and scanning electron microscope imaging. *J Strain Anal Eng Des* 43 (8):719–728. doi:10.1243/03093247JSA412
37. Sutton MA, Li N, Joy DC, Reynolds AP, Li X (2007) Scanning electron microscopy for quantitative small and large deformation measurements Part I: SEM imaging at magnifications from 200 to 10,000. *Exp Mech* 47(6):775–787. doi:10.1007/s11340-007-9042-z
38. Muskhelishvili NL (1977) *Some Basic Problems of the Mathematical Theory of Elasticity,* Leyden, the Netherlands: Noordhoff Groningen
39. Pelletier JM, Yokoyama Y, Inoue A (2007) Dynamic mechanical properties in a Zr₅₀Cu₄₀Al₁₀ bulk metallic glass. *Mater Trans* 47:1359–1362. doi:10.2320/matertrans.MF200626
40. Schajer GS, Altus E (1996) Stress calculation error analysis for incremental hole-drilling residual stress measurements. *ASME J Eng Mater Technol* 118(1):120–126
41. Zucarello B (1999) Optimal calculation steps for the evaluation of residual stress by the incremental hole-drilling method. *Exp Mech* 39(2):117–124. doi:10.1007/BF02331114
42. Schajer GS, Prime MB (2006) Use of inverse solutions for residual stress measurements. *J Eng Mater Technol-Transactions of the ASME* 128(3):375–382. doi:10.1115/1.2204952
43. Neubauer A (1997) On converse and saturation results for Tikhonov regularization of linear ill-posed problems. *SIAM J Numer Anal* 34(2):517–527
44. Lamm PK, Elden L (1997) Numerical solution of first-kind Volterra equations by sequential Tikhonov regularization. *SIAM J Numer Anal* 34(4):1432–1450
45. Beck JV, Blackwell B, St.Clair CR Jr (1985) *Inverse heat conduction - Ill-posed problems.* Wiley-Interscience, New York
46. Prime MB, Hill MR (2006) Uncertainty, model error, and order selection for series-expanded, residual-stress inverse solutions. *ASME J Eng Mater Technol* 128(2):175–185. doi:10.1115/1.2172278